Dalton Transactions

ROYAL SOCIETY OF CHEMISTRY

PAPER

View Article Online
View Journal | View Issue

Check for updates

Cite this: *Dalton Trans.*, 2020, **49**, 8693

Allosteric regulation of rotational, optical and catalytic properties within multicomponent machinery†

Suchismita Saha,[a] Amit Ghosh,[a] Thomas Paululat[b] and Michael Schmittel *[a]

Received 1st June 2020,
Accepted 9th June 2020

DOI: 10.1039/d0dt01961e

rsc.li/dalton

The reversible transformation of multicomponent nanorotors (**ROT-1**, k_{298} = 44 kHz or **ROT-2**, k_{298} = 61 kHz) to the "dimeric" supramolecular structures (**DS-1** or **DS-2**, k_{298} = 0.60 kHz) was triggered by a stoichiometric chemical stimulus. Simple coordination changes at the central phenanthroline of the molecular device by altering metal ions ($Cu^{+} \rightarrow Zn^{2+}$) or stoichiometry ($Cu^{+}$, 1 equiv. → 0.5 equiv.) affected the terminal zinc(II) porphyrin units, the active sites within the machinery, changing rotational, catalytic and optical properties. In presence of added pyrrolidine, the nanorotor **ROT-1** was inactive for catalysis whereas formation of the dimeric supramolecular structures **DS-1** initiated a Michael addition reaction by releasing the organocatalyst from the porphyrin sites. This catalytic machinery (**ROT-1** ⇄ **DS-1**) proved to reproducibly work over two full cycles using allosteric OFF/ON control of catalysis.

Introduction

Coordination-driven structural rearrangements[1,2] of supramolecular architectures[3–7] have been recently utilized to control catalytic reactions[8–11] and guest uptake/release.[3a,12–15] Whereas examples of allosteric regulation[16–21] are abundant for controlling functions, even in supramolecular constructs, very few examples are known where a multitude of functions is tuned allosterically.[22–24]

Most of the literature-known allosteric regulation has been performed using covalent receptors.[20,25,26] However, in biological systems, a remarkable amount of proteins showing allosteric regulation of their enzymatic activity are multicomponent in nature.[27,28] Some of these cases demonstrate that small molecular effectors allow or inhibit allosteric enzymatic regulation through control of dimerization (Fig. 1). For instance, the enzyme ATP phosphoribosyltransferase is active in its dimeric state and allosterically inhibited by added histidine triggering a transformation of the active dimeric into an inactive hexameric form.[27,29]

Herein, we demonstrate how reversible allosteric regulation[30] allows parallel control of three functions: ON/OFF catalysis, OFF/ON rotor operation and UP/DOWN fluorescence changes upon moving from a multicomponent monomeric assembly to a dimeric system by addition of small molecular effectors. The key to reach such multifunctional control is the stoichiometric and reversible coordination-driven transformation of a three-component nanorotor (2 equiv.) into a three-component dimeric and dynamic supramolecule (1 equiv.). The main components of both supramolecular self-assemblies are ligand **1**, a phenanthroline carrying two distal zinc(II) porphyrin units, and the bis-pyridine bipeds **2a**,**b** (Fig. 2). Indeed, this seems to be the first example of allosterically controlling multiple functions in parallel within a multicomponent machinery requiring dimerization of structures.

In detail, either by changing the stoichiometry of the metal ion (Cu^{+}) or the metal ion itself ($Cu^{+} \rightarrow Zn^{2+}$) the coordinative situation at the central phenanthroline site in $[Cu(\mathbf{1})(\mathbf{2a})]^{+}$ (**ROT-1**) or $[Cu(\mathbf{1})(\mathbf{2b})]^{+}$ (**ROT-2**) was changed which regulated the binding mode at the terminal zinc(II) porphyrin (ZnPor) units providing quantitative and reversible interconversion of nanorotor (**ROT-1**/**ROT-2**) ⇄ "dimeric" supramolecule (**DS-1**/**DS-2**) (Fig. 3). This device-to-dimer transformation was used

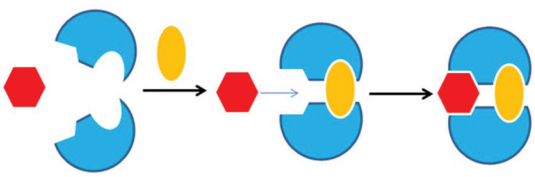

Fig. 1 Formation of the active site by the dimerization of two protein molecules.[27]

[a]*Center of Micro- and Nanochemistry and Engineering, Department Chemie – Biologie, Organische Chemie I, Adolf–Reichwein–Str. 2, D-57068 Siegen, Germany. E-mail: schmittel@chemie.uni-siegen.de*
[b]*Department Chemie – Biologie, Organische Chemie II, Adolf–Reichwein–Str. 2, D-57068 Siegen, Germany*

†Electronic supplementary information (ESI) available. See DOI: 10.1039/d0dt01961e

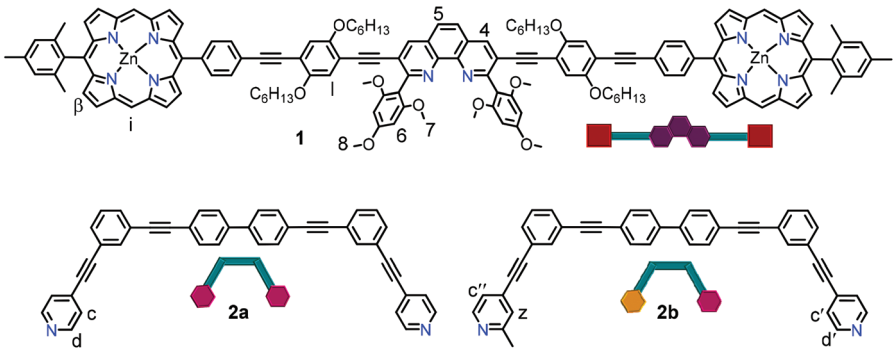

Fig. 2 Chemical structure of ligands **1**, **2a** and **2b** along with their cartoon representations.

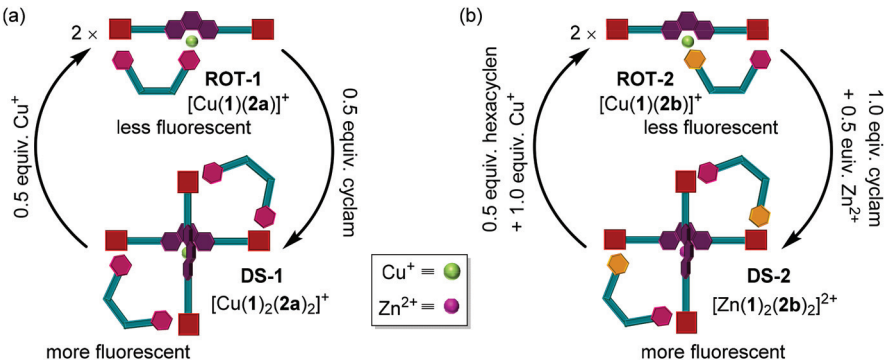

Fig. 3 Cartoon representation of the reversible transformations between nanorotor **ROT-1**/**ROT-2** → dimeric supramolecules **DS-1**/**DS-2**.

for controlling the liberation of a catalyst from the ZnPor binding site into the solution hence regulating OFF/ON catalysis. The switchable ensemble thus constitutes catalytic machinery.

Results and discussion

Design

For the required stoichiometry-dependent self-sorting, ligand **1** was designed. It contains two terminal ZnPor sites and one central phenanthroline unit so that its metal complexes can act as stator ($[Cu(\mathbf{1})]^+$) or decks ($[Cu(\mathbf{1})_2]^+$ and $[Zn(\mathbf{1})_2]^{2+}$) in either the rotor or the dimeric supramolecule, respectively (Fig. 3).[8c,31] The heart of ligand **1** was conceived as a 2,9-bis (2,4,6-trimethoxyphenyl)-1,10-phenanthroline unit (*vide infra*). We have chosen the 2,4,6-trimethoxyphenyl substitution at the 2,9-position of phenanthroline because it was expected to provide the optimal electronic stabilization and steric bulk to quantitatively afford the coordinatively frustrated complex $[Cu(\mathbf{1})]^+$ (with copper(I) in a 1 : 1 ratio), while the 2 : 1 mixture should furnish complex $[Cu(\mathbf{1})_2]^+$. Phenanthrolines without or with too bulky substituents, *e.g.*, mesityl rings at the 2,9-position of phenanthroline, do not exhibit the plasticity of forming 2 : 1 and 1 : 1 complexes with Cu^+ depending on the stoichiometry.[32]

Model studies

In order to ascertain the final design of ligands **1** and **2**, we have performed model studies to prove the orthogonality between the $[Cu(\mathbf{1})_2]^+$ complexation and the N_{py} → ZnPor binding. For this purpose, ligands **3**, **4**, **5**, and $[Cu(CH_3CN)_4]PF_6$ (2 : 1 : 1 : 1) were dissolved in CD_2Cl_2 in an NMR tube (Fig. 4a). The comparison of characteristic ^{1}H NMR signals of the phenanthroline (3′-, 4′-, 5′-, 6′-H), pyridine (2-H) and porphyrin (i′-, β′-H) units with those in the individual complexes sustained quantitative formation of the two non-interfering complexes $[Cu(\mathbf{3})_2]^+$ and **4**·**5** (Fig. 4b).

Synthesis and characterization of 1, 2a and 2b

Ligands **1**, **2a** and **2b** were prepared in multistep approaches (see ESI†). The Sonogashira coupling reaction of 3,8-diethynyl-2,9-bis(2,4,6-trimethoxyphenyl)-1,10-phenanthroline and zinc(II) 5-iodophenyl-15-mesitylporphyrin afforded ligand **1** in 75% yield. The symmetric biped **2a** was synthesized by Sonogashira coupling between 4,4′-bis((3-ethynylphenyl)ethynyl)biphenyl and 4-iodopyridine in the final step. The dissymmetric biped **2b** was prepared by stepwise Sonogashira couplings of 4,4′-bis ((3-ethynylphenyl)ethynyl)biphenyl with 4-iodopyridine and 4-bromopicoline, respectively. All the ligands were unambiguously characterized by ^{1}H NMR, ^{1}H–^{1}H COSY, ^{13}C NMR, ESI-MS and elemental analysis (see ESI†).

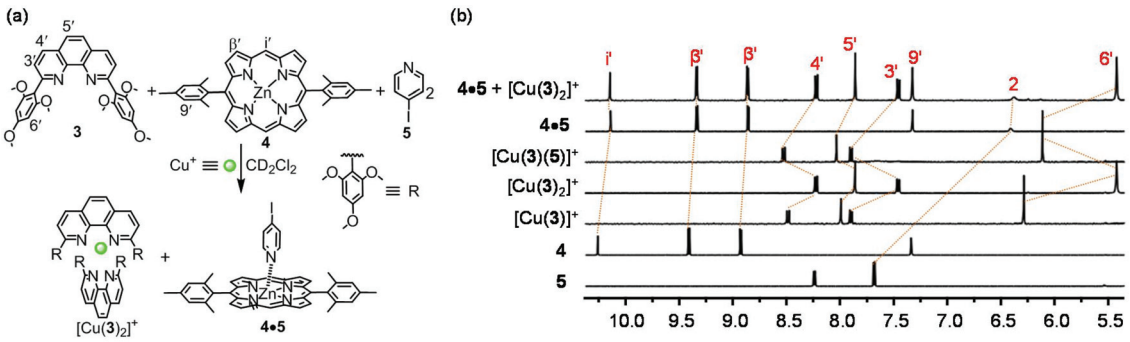

Fig. 4 (a) Orthogonality between complexes $[Cu(\mathbf{3})_2]^+$ and **4·5**. (b) Partial ^{1}H NMR (400 MHz, CD_2Cl_2, 295 K) of **5**, **4**, $[Cu(\mathbf{3})]^+$, $[Cu(\mathbf{3})_2]^+$, $[Cu(\mathbf{3})(\mathbf{5})]^+$, **4·5** and **4·5** + $[Cu(\mathbf{3})_2]^+$.

Preparation of metal complexes, rotors and dimeric supramolecules

Alike the model compound **3**, ligand **1** can form both the coordinatively frustrated Cu^+ complex $[Cu(\mathbf{1})]^+$ and the bishomoleptic complex $[Cu(\mathbf{1})_2]^+$ based on the relative stoichiometry. Significant chemical shifts in the ^{1}H NMR signal of protons 6-H, l-H and other phenanthroline protons in ligand **1**, $[Cu(\mathbf{1})]^+$ and $[Cu(\mathbf{1})_2]^+$ supported quantitative formation of the complexes (Fig. 5a and ESI, Fig. S49†). Considerable upfield shift of protons 6-H, 7-H, 8-H and l-H in complex $[Cu(\mathbf{1})_2]^+$ were attributed to the π-ring current arising from the 2,4,6-trimethoxyphenyl units.

Due to the precise stoichiometry-dependent self-sorting, **ROT-1** = $[Cu(\mathbf{1})(\mathbf{2a})]^+$ (Fig. 3a) was quantitatively formed by mixing **1**, **2a** and $[Cu(CH_3CN)_4]PF_6$ (1 : 1 : 1) in CD_2Cl_2, irrespective of the sequence. In nanorotor **ROT-1**, $[Cu(\mathbf{1})]^+$ acts as the stator holding the rotator **2a** *via* $N_{py} \rightarrow [Cu(phenAr_2)]^+$ (= HETPYP-I: HETeroleptic PYridine and Phenanthroline complexation)[33] and $N_{py} \rightarrow$ ZnPor binding. Upfield shifts of proton signals i-H, 6-H and l-H from 10.34 to 10.28 ppm, 6.40 to 6.32 ppm and 6.70 to 6.64 ppm in the ^{1}H NMR unambiguously attested the binding of **2a** to $[Cu(\mathbf{1})]^+$ (Fig. 5a). As monitored in the UV-vis spectrum, the red shift of the Q-band of the ZnPor from 537 to 540 nm when going from **1** to **ROT-1** = $[Cu(\mathbf{1})(\mathbf{2a})]^+$ manifested the axial binding of one pyridine foot of **2a** to the ZnPor units of $[Cu(\mathbf{1})]^+$ (Fig. 5b). Moreover, a single peak in the ESI-MS at m/z = 1457.8 and a single set of ^{1}H-DOSY signals corroborated the formation of **ROT-1** (ESI, Fig. S76 & S60†).

Quantitative formation of the dimeric supramolecular structure **DS-1** = $[Cu(\mathbf{1})_2(\mathbf{2a})_2]^+$ was achieved by mixing **1**, **2a** and $[Cu(CH_3CN)_4]PF_6$ in a 1 : 1 : 0.5 ratio in CD_2Cl_2 (Fig. 3a). In the ^{1}H NMR, protons 6-H and l-H along with all other phenanthroline protons appeared at the same position as in the homoleptic complex $[Cu(\mathbf{1})_2]^+$ that represents the deck for both bipeds in **DS-1** (Fig. 5a). Upfield shift of proton signal i-H (10.34 to 10.22 ppm), d-H (8.60 to 2.35 ppm) and c-H (7.41 to 5.52 ppm) when going from $[Cu(\mathbf{1})_2]^+$ to **DS-1** confirmed binding of **2a** ($N_{py} \rightarrow$ ZnPor) (Fig. 5a and ESI, Fig. S49†). In the UV-vis the red shift of the Q-band of the ZnPor unit from 537 to 543 nm (for **1** → **DS-1**) supported the $N_{py} \rightarrow$ ZnPor axial binding of **2a** in $[Cu(\mathbf{1})_2]^+$ (Fig. 5b). Formation of **DS-1** was further confirmed by ESI-MS and ^{1}H DOSY NMR (ESI, Fig. S77 and S61†).

In **ROT-1**, one of the pyridine feet of the rotating biped is always attached to the central copper(I) phenanthroline thereby representing an axle for the other pyridine site that oscillates between both degenerate zinc porphyrins of the stator (*cf.* 50% loading of the ZnPor units). In contrast, in **DS-1** all ZnPor sites are constantly occupied by the pyridine sites of the bipeds due to the pyridine : ZnPor ratio of 1 : 1. The strong $N_{py} \rightarrow$ ZnPor axial binding in **DS-1** was clearly supported by

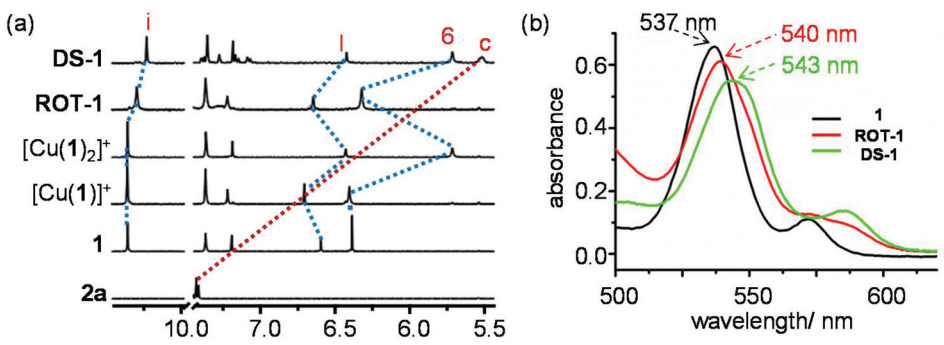

Fig. 5 (a) Partial ^{1}H NMR (400 MHz, CD_2Cl_2, 295 K) of **2a**, **1**, $[Cu(\mathbf{1})]^+$, $[Cu(\mathbf{1})_2]^+$, **ROT-1** and **DS-1**. (b) UV-vis spectra of **1**, **ROT-1** and **DS-1** in CH_2Cl_2 at 298 K ($c = 10^{-5}$ M).

the upfield shift of proton signal i-H (10.28 to 10.22 ppm) in the ^{1}H NMR and the red shift of the Q-band (Fig. 5) of the ZnPor sites (540 → 543 nm) in the UV-vis when going from **ROT-1** (50% loading of the ZnPor sites by the pyridine foot of **2a**) to **DS-1** (full loading of the ZnPor sites by the pyridine foot of **2a**).

Similarly, the 1 : 1 : 1 mixture of **1**, $[Cu(CH_3CN)_4]PF_6$ and **2b** led to quantitative formation of **ROT-2** = $[Cu(\mathbf{1})(\mathbf{2b})]^+$ where the picoline site of **2b** was bound selectively to the copper(I) phenanthroline unit of $[Cu(\mathbf{1})]^+$ through HETPYP-I[33] interaction (Fig. 3b). The selective binding originated from the *ortho*-methyl substitution at the pyridine which increased the strength of the HETPYP-coordination to $\log K_{pic}$ = 5.86 (ESI, Fig. S83†) and weakened the N_{pic} → ZnPor interaction ($\log K_{pic}$ = 2.72) due to steric crowding.[8b,34] The upfield shift in the ^{1}H NMR of proton signals 6-H, l-H and i-H from $[Cu(\mathbf{1})]^+$ → $[Cu(\mathbf{1})(\mathbf{2b})]^+$ proved the interaction between **2b** and $[Cu(\mathbf{1})]^+$ which was further verified by the red-shift of the Q-band (from 537 to 540 nm) (Fig. 6 and ESI, Fig. S86†). Formation of **ROT-2** was additionally confirmed by ^{1}H DOSY and ESI-MS data (ESI, Fig. S62 and S78†).

Unlike **DS-1**, mixing of **1**, **2b** and Cu^+ in 1 : 1 : 0.5 ratio did not quantitatively furnish the dimeric supramolecular structure $[Cu(\mathbf{1})_2(\mathbf{2b})_2]^+$. Alike, using the model ligands there was no 100% orthogonality between $[Cu(\mathbf{3})_2]^+$ and N_{pic} → ZnPor binding. In comparison with **ROT-2**, the picoline group of biped **2b** has to sacrifice in $[Cu(\mathbf{1})_2(\mathbf{2b})_2]^+$ the strong HETPYP binding at the $[Cu(phenAr_2)]^+$ unit in **ROT-2** ($\log K_{pic}$ = 5.86) for the weak one at the ZnPor site in $[Cu(\mathbf{1})_2(\mathbf{2b})_2]^+$ ($\log K_{pic}$ = 2.72). Such loss in driving force cannot be compensated by formation of the central $[Cu(\mathbf{1})_2]^+$ unit. The thermodynamics, however, can be remedied by using Zn^{2+} instead of Cu^+ owing to its stronger bishomoleptic complexes with ligands of type **3** (ESI, Fig. S41†). The self-assembly **DS-2** = $[Zn(\mathbf{1})_2(\mathbf{2b})_2]^{2+}$ was indeed quantitatively furnished by mixing **1**, **2b** and Zn^{2+} in 1 : 1 : 0.5 ratio (Fig. 3b). Its formation was unambiguously proved by ^{1}H NMR, ESI-MS and elemental analysis (ESI, page S29–30†). For instance, in the ^{1}H NMR (CD_2Cl_2), the splitting of proton signal 6-H into four singlets (6′, 6″, 6‴ and 6⁗-H) and l-H into two singlets (l′ and l″-H) like $[Zn(\mathbf{1})_2]^{2+}$, the upfield shifts of c″-H (7.22 to 6.15 ppm) and c′-H (7.42 to 5.63 ppm) from free **2b** verified the formation of **DS-2** (Fig. 6).

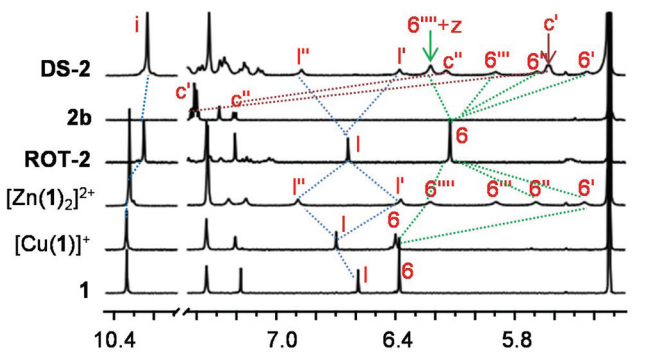

Fig. 6 Partial ^{1}H NMR (400 MHz, CD_2Cl_2, 295 K) of **1**, $[Cu(\mathbf{1})]^+$, $[Zn(\mathbf{1})_2]^{2+}$, **ROT-2**, **2b** and **DS-2**.

Dynamic VT-NMR

After successfully realizing quantitative formation of new dynamic multicomponent structures, we were interested to determine their exchange processes, exchange frequencies and activation parameters. The single set of protons for both porphyrin units in rotors **ROT-1** and **ROT-2** in the ^{1}H NMR attested fast rotation on the ^{1}H NMR timescale.

VT ^{1}H NMR of **ROT-1** was performed from 25 °C to −70 °C and changes in the signal of proton i-H served for analyzing the kinetic data (Fig. 7a). It appeared as a sharp singlet at 25 °C (10.28 ppm) but split into a 1 : 1 set at −70 °C (10.33 and 10.22 ppm). The signal at 10.22 ppm was assigned to the pyridine-coordinated ZnPor whereas the signal at 10.33 ppm was allocated to the free ZnPor unit. Rotational exchange frequencies (k) at different temperatures were calculated using WinDNMR[35] which provided the exchange frequency at room temperature k_{298} = 44 kHz. Activation parameters were derived from the Eyring plot (ESI, Fig. S57†) and are provided in Table 1.

The VT ^{1}H NMR of **ROT-2**, recorded from 25 °C to −50 °C, exhibited a splitting of the sharp singlet of proton i-H into a set of two singlets (1 : 1) with a coalescence temperature at −30 °C (Fig. 7b). As before, the corresponding activation parameters were determined (Table 1). The exchange frequency at room temperature was calculated as k_{298} = 61 kHz.

As in **DS-1** all binding sites (N_{py} → ZnPor) are identical, even after freezing, the exchange cannot be monitored. To determine the kinetic parameters of such a process, the dissymmetric arm **2b** was used in **DS-2** with pyridine at one terminal and picoline at the other end.

The single set of all porphyrin protons in **DS-2** manifested fast exchange on the NMR time scale at room temperature. Upon lowering the temperature, the VT ^{1}H-NMR of **DS-2** (Fig. 7c) exhibited a splitting of proton signal β-H (1 : 1). Exchange frequencies (k) at different temperatures provided the activation parameters (Table 1) and k_{298} = 0.60 kHz.

The much lower speed in the dynamic dimeric supramolecule than that of the rotors can be easily understood by their distinct mechanisms. In the rotors **ROT-1** and **ROT-2**, the rate determining step for rotation comprises the single detachment of the N_{py} axial coordination from the ZnPor unit,[8c] leading to an exchange rate $k_{ex} = \frac{1}{2}k_{diss}$ ($\frac{1}{2}$ is a statistical factor recognizing that one out of two re-attachments will lead to exchange of both site). In contrast, the mechanism of exchange in **DS-2** is quite different. Firstly, in **DS-2** all sites are loaded and, secondly, only the exchange of pyridine by a picoline at a given ZnPor site or *vice versa* is detected by NMR. Based on the highly positive activation entropy and the high activation enthalpy there is a possibility that the exchange proceeds by full dissociation/re-association of one biped.

Interconversion

After the preparation of the individual parts of the machinery (**ROT-1**/**ROT-2** and **DS-1**/**DS-2**) with their highly different dynamic properties, our next target was to interconvert them using chemical input. As their ^{1}H NMR and fluorescence

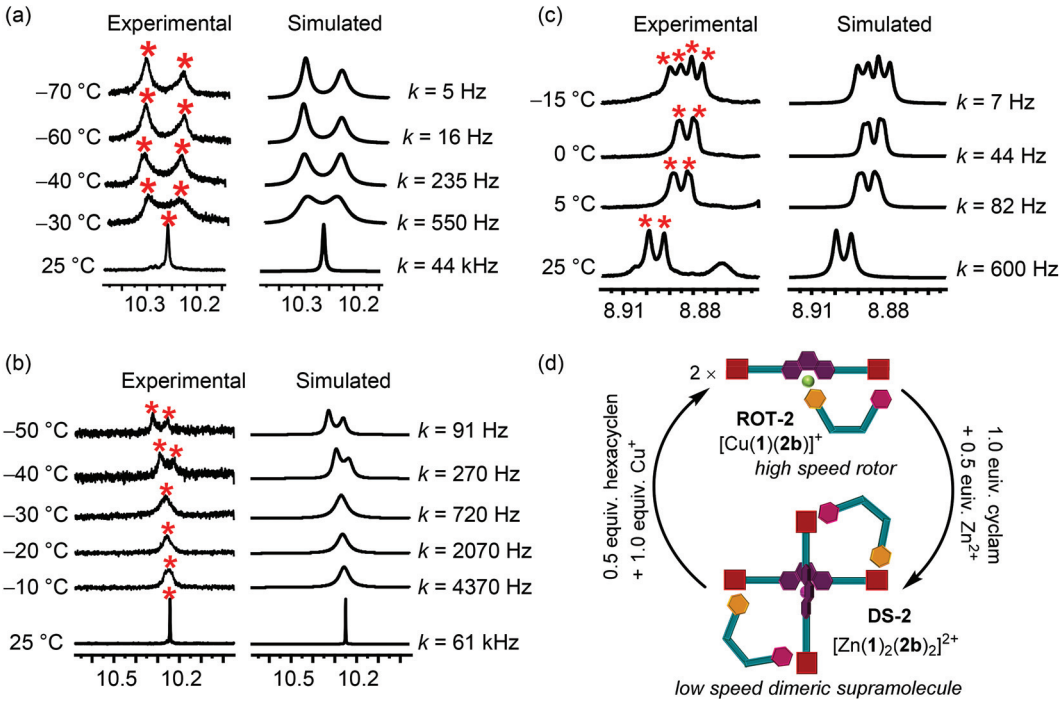

Fig. 7 VT-^{1}H NMR (600 MHz, CD_2Cl_2) of (a) **ROT-1** and (b) **ROT-2** displaying the splitting of proton signal i-H into 1 : 1 ratio. (c) VT-^{1}H NMR (600 MHz, CD_2Cl_2) of **DS-2** showing the splitting (two sets: 1 : 1) of proton signal β-H. (d) Cartoon representation showing reversible transformation of the high-speed nanorotor to the dynamic low-speed **DS-2**.

Table 1 Exchange frequencies in **ROT-1**, **ROT-2** and **DS-2** along with the activation parameters

Nanomachines	k_{298}/ kHz	$\Delta H^{\ddagger}$/ kJ mol^{-1}	$\Delta S^{\ddagger}$/ J mol^{-1} K^{-1}	$\Delta G^{\ddagger}_{298}$/ kJ mol^{-1}
ROT-1	44	46.5 ± 1.2	0.6 ± 0.2	46.3 ± 1.2
ROT-2	61	46.1 ± 0.5	1.4 ± 0.9	45.7 ± 0.2
DS-2	0.60	68.9 ± 3.6	43.1 ± 3.6	57.2 ± 0.2

spectra proved to be different, interconversion was monitored by both emission and ^{1}H NMR spectroscopy.

At first, the dimeric supramolecule **DS-1** was prepared by mixing ligands **1**, **2a** and Cu^+ (1 : 1 : 0.5). Its formation was confirmed by ^{1}H NMR and fluorescence spectroscopy. Further addition of 0.5 equiv. of $[Cu(CH_3CN)_4]PF_6$ to **DS-1**, hence changing the stoichiometry of Cu^+ : **1** from 0.5 : 1 to 1 : 1, quantitatively generated nanorotor **ROT-1** as validated by spectroscopic data. The transformation of the dimeric supramolecule to a "monomeric" rotor was possible by changing the tetracoordinated homoleptic copper(I) center at the central phenanthroline to a tricoordinated HETPYP-I center. Addition of 0.5 equiv. of cyclam to **ROT-1** regenerated **DS-1** by removing a stoichiometric amount of Cu^+ as cyclam is a stronger chelating agent for Cu^+ than phenanthroline.[3b,8b] Three complete cycles interconverting **DS-1** ⇄ **ROT-1** were performed and monitored by fluorescence and NMR spectroscopy (Fig. 8a, c and ESI, Fig. S50†).

The kinetics of the interconversion was followed by fluorescence. Ligand **1**, **DS-1** and **ROT-1** exhibit typical ZnPor emission patterns with different intensity. In the free ligand, the fluorescence intensity is highest followed by that in **DS-1** and in **ROT-1** (Fig. 8a). Conversion of **DS-1** to **ROT-1** took 12 min whereas **ROT-1** to **DS-1** was finished within 6 min at room temperature, $c = 10^{-5}$ M (Fig. 8c).

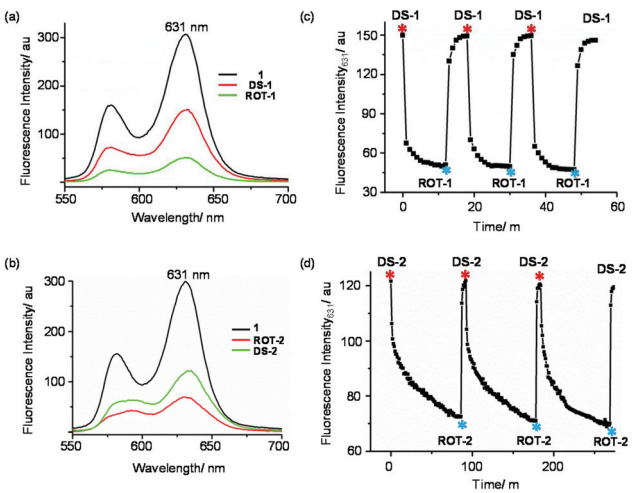

Fig. 8 Fluorescence spectra of (a) **1**, **ROT-1**, **DS-1** and (b) **1**, **ROT-2**, **DS-2** in CH_2Cl_2 at 298 K (λ_{exc} = 540 nm, $c = 10^{-5}$ M). Fluorescence intensity changes (λ_{em} = 631 nm) *vs.* time over three cycles for (c) **DS-1** → **ROT-1** and (d) **DS-2** → **ROT-2** in CH_2Cl_2 at 298 K (λ_{exc} = 540 nm, $c = 10^{-5}$ M). Copper(I) and cyclam additions are shown by red and indigo asterisk, respectively, in Fig. 8c. Additions of hexacyclen + Cu^+ (1 : 2) and cyclam + Zn^{2+} (2 : 1) are shown by red and indigo asterisk, respectively, in Fig. 8d.

In order to investigate the interconversion of **DS-2** → **ROT-2**, we first prepared **DS-2** by mixing **1**, **2b** and Zn^{2+} (1 : 1 : 0.5). Addition of 0.5 equiv. of hexacyclen and 1.0 equiv. of Cu^{+} transformed the dimeric supramolecule **DS-2** into the monomeric nanorotor **ROT-2** by selective interchange of the metal ion at the central phenanthroline station.[8a,c,22] Now, addition of 1.0 equiv. of cyclam and 0.5 equiv. of Zn^{2+} regenerated **DS-2** by "dimerization" of the nanorotor. Three complete interconversion cycles were successfully carried out in a highly reproducible manner as demonstrated by fluorescence and ^{1}H NMR data (Fig. 8b, d and ESI, Fig. S56†).

Equally, the kinetic course of the interconversion was evaluated by fluorescence (Fig. 8d). The conversion of **DS-2** to **ROT-2**, triggered by addition of 0.5 equiv. of hexacyclen and 1.0 equiv. of Cu^{+}, took around 85 min whereas the transformation **ROT-2** → **DS-2** was completed within 6 min after addition of 1.0 equiv. of cyclam and 0.5 equiv. of Zn^{2+} at room temperature.

Catalysis

The stoichiometry-driven interconversion of the supramolecular rotor to dimeric structure goes along with distinct changes in nanomechanical motions and optical properties. Our focus though was to set up catalytic machinery requiring control of the ON/OFF catalytic activity of the interconverting system by allosteric release and capture of a catalytically active guest at the zinc(II) porphyrin center. Hereunto, the key is the structural rearrangement at the central phenanthroline site that triggers conformational/constitutional changes as the ZnPor sites. After several tests, we identified the parent pyrrolidine (**6**) as the best candidate because binding of **6** to ZnPor is strong enough ($\log K_{pyrr}$ = 4.90 ± 0.20) to be seized by **ROT-1** (1 : 1 ratio of **ROT-1** and **6**) whereas it is freed in **DS-1** for catalysis (ESI, Fig. S84†). Model reactions of Michael acceptor **7** (100 mol%) and nucleophile **8** (2000 mol%) in CD_2Cl_2 : $CDCl_3$ (20 : 1) with **6** (10 mol%) as catalyst provided (42 ± 1)% of product **9** after 4 h (at 50 °C) (Fig. 9a and ESI, Fig. S89†). In contrast, a (1 : 1) mixture of model zinc porphyrin **4** and catalyst **6** (10 mol%) furnished no product under identical reaction conditions due to the strong binding of the catalyst in the ZnPor complex **4·6** (ESI, Fig. S90†). When 10 mol% of **6·ROT-1** (1 : 1 mixture of **ROT-1** and **6**) were used as catalyst in the above Michael addition reaction, similarly no product formed, as **6** was sufficiently bound at the ZnPor unit of **ROT-1** (ESI, Fig. S91†). This state we denote as the catalytic OFF state. For the catalytic ON state now **DS-1** (5 mol%) + 2 × **6** were used which furnished (39 ± 1)% of product **9** under identical reaction conditions (ESI, Fig. S92†). Importantly, we observe basically identical catalytic activity with **DS-1** (39%) as with the free catalyst in the model system (42%). Apparently, all added catalyst **6** is available for catalysis in **DS-1**.

After testing in separate steps the function of the catalytic ON and OFF states, allosteric catalytic cycles were performed starting with the OFF state composed of 10 mol% **6·ROT-1**, **7** (100 mol%) and **8** (2000 mol%) affording no product **9** after 4 h at 50 °C (Fig. 9b and ESI, Fig. S93†). Addition of cyclam (5 mol%) should remove an equimolar amount of Cu^{+} from the system furnishing 5 mol% of **DS-1** which was expected to allosterically release the guest catalyst **6** from the ZnPor stations into solution because all ZnPor sites are now intrasupramolecularly loaded with biped **2a**. Indeed, addition of 5 mol% of cyclam to the OFF state provided 39% of product **9** after 4 h at 50 °C. After realizing this ON catalytic state, consumed amount of substrates and 5 mol% of $[Cu(CH_3CN)_4]PF_6$ were added. Heating at 50 °C for 4 h did not provide any further product formation, hence proving that this is an OFF state. Addition of 5 mol% of $[Cu(CH_3CN)_4]PF_6$ to the ON state converted the dimeric supramolecule **DS-1** to nanorotor **ROT-1** with one ZnPor station free to capture all the guest catalyst **6**, making it unavailable for the catalytic reaction. Two complete OFF/ON catalytic cycles were performed to demonstrate the ability of the full catalytic machinery in allosterically controlling the uptake/release of the guest catalyst (Fig. 9b).

In conclusion we have demonstrated the stoichiometry and coordination-driven reversible transformation of a multicomponent nanorotor to dimeric supramolecule by changing the coordination mode at the central phenanthroline unit. As a result of this interconversion within the machinery, allosteric

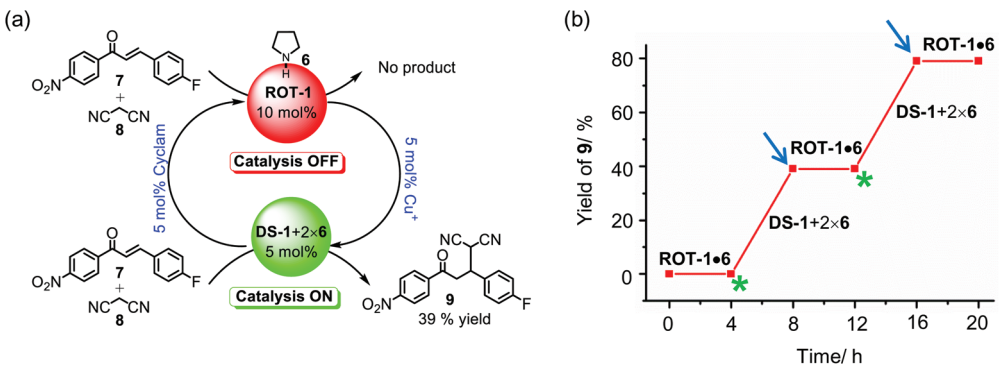

Fig. 9 (a) Representation of the OFF/ON regulation of the pyrrolidine-catalyzed Michael addition involving the reversible interconversion within the catalytic machinery **ROT-1** ⇄ **DS-1** by removal and addition of Cu^{+}. (b) Two complete catalytic cycles were performed between **ROT-1** and **DS-1** in presence of pyrrolidine (**6**). The instant of cyclam addition is shown by green asterisk, whereas Cu^{+} and consumed substrate addition are indicated by blue arrow.

tuning of OFF/ON rotor formation, UP/DOWN fluorescence and ON/OFF of Michael addition catalysis was achieved over two cycles.

This work demonstrates that self-sorting[36] in combination with allosteric tuning of binding events is a powerful tool for realizing multifunctional machinery.

Conflicts of interest

There are no conflicts to declare.

Acknowledgements

We are indebted to the University of Siegen and the Deutsche Forschungsgemeinschaft for continued support under Schm 647/20-2. Dedicated to Prof. Dr Günther von Bünau (Siegen) on the occasion of his 90th birthday.

References

1 W. Wang, Y.-X. Wang and H.-B. Yang, *Chem. Soc. Rev.*, 2016, **45**, 2656–2693.
2 C. G. Oliveri, P. A. Ulmann, M. J. Wiester and C. A. Mirkin, *Acc. Chem. Res.*, 2008, **41**, 1618–1629.
3 (*a*) I. Paul, D. Samanta, S. Gaikwad and M. Schmittel, *Beilstein J. Org. Chem.*, 2019, **15**, 1371–1378; (*b*) N. Mittal, M. L. Saha and M. Schmittel, *Chem. Commun.*, 2016, **52**, 8749–8752; (*c*) M. L. Saha and M. Schmittel, *Inorg. Chem.*, 2016, **55**, 12366–12375.
4 R. Zhu, J. Lübben, B. Dittrich and G. H. Clever, *Angew. Chem., Int. Ed.*, 2015, **54**, 2796–2800.
5 V. E. Campbell, X. de Hatten, N. Delsuc, B. Kauffmann, I. Huc and J. R. Nitschke, *Nat. Chem.*, 2010, **2**, 684–687.
6 K. Harano, S. Hiraoka and M. Shionoya, *J. Am. Chem. Soc.*, 2007, **129**, 5300–5301.
7 J.-P. Collin, C. Dietrich-Buchecker, P. Gaviña, M. C. Jimenez-Molero and J.-P. Sauvage, *Acc. Chem. Res.*, 2001, **34**, 477–487.
8 (*a*) A. Goswami, T. Paululat and M. Schmittel, *J. Am. Chem. Soc.*, 2019, **141**, 15656–15663; (*b*) N. Mittal, M. S. Özer and M. Schmittel, *Inorg. Chem.*, 2018, **57**, 3579–3586; (*c*) A. Goswami, S. Pramanik and M. Schmittel, *Chem. Commun.*, 2018, **54**, 3955–3958; (*d*) S. Gaikwad, A. Goswami, S. De and M. Schmittel, *Angew. Chem., Int. Ed.*, 2016, **55**, 10512–10517.
9 G.-H. Ouyang, Y.-M. He, Y. Li, J.-F. Xiang and Q.-H. Fan, *Angew. Chem., Int. Ed.*, 2015, **54**, 4334–4337.
10 J. T. Foy, D. Ray and I. Aprahamian, *Chem. Sci.*, 2015, **6**, 209–213.
11 C. M. McGuirk, J. Mendez-Arroyo, A. M. Lifschitz and C. A. Mirkin, *J. Am. Chem. Soc.*, 2014, **136**, 16594–16601.
12 S. Bandi, A. K. Pal, G. S. Hanan and D. K. Chand, *Chem. – Eur. J.*, 2014, **20**, 13122–13126.
13 N. Kishi, M. Akita and M. Yoshizawa, *Angew. Chem., Int. Ed.*, 2014, **53**, 3604–3607.
14 N. C. Gianneschi, M. S. Masar and C. A. Mirkin, *Acc. Chem. Res.*, 2005, **38**, 825–837.
15 S. Hiraoka, K. Harano, M. Shiro and M. Shionoya, *Angew. Chem., Int. Ed.*, 2005, **44**, 2727–2731.
16 V. Marti-Centelles, R. L. Spicer and P. J. Lusby, *Chem. Sci.*, 2020, **11**, 3236–3240.
17 (*a*) C. M. McGuirk, J. Mendez-Arroyo, A. I. d'Aquino, C. L. Stern, Y. Liu and C. A. Mirkin, *Chem. Sci.*, 2016, **7**, 6674–6683; (*b*) C. M. McGuirk, C. L. Stern and C. A. Mirkin, *J. Am. Chem. Soc.*, 2014, **136**, 4689–4696; (*c*) J. Mendez-Arroyo, J. Barroso-Flores, A. M. Lifschitz, A. A. Sarjeant, C. L. Stern and C. A. Mirkin, *J. Am. Chem. Soc.*, 2014, **136**, 10340–10348; (*d*) H. J. Yoon, J. Kuwabara, J.-H. Kim and C. A. Mirkin, *Science*, 2010, **330**, 66–69; (*e*) N. C. Gianneschi, P. A. Bertin, S. T. Nguyen, C. A. Mirkin, L. N. Zakharov and A. L. Rheingold, *J. Am. Chem. Soc.*, 2003, **125**, 10508–10509.
18 S. Freye, J. Hey, A. Torras-Galan, D. Stalke, R. Herbst-Irmer, M. John and G. H. Clever, *Angew. Chem., Int. Ed.*, 2012, **51**, 2191–2194.
19 M. Schmittel, S. Pramanik and S. De, *Chem. Commun.*, 2012, **48**, 11730–11732.
20 L. Kovbasyuk and R. Krämer, *Chem. Rev.*, 2004, **104**, 3161–3187.
21 M. Ayabe, A. Ikeda, S. Shinkai, S. Sakamoto and K. Yamaguchi, *Chem. Commun.*, 2002, 1032–1033.
22 A. Goswami, I. Paul and M. Schmittel, *Chem. Commun.*, 2017, **53**, 5186–5189.
23 A. Faulkner, T. van Leeuwen, B. L. Feringa and S. J. Wezenberg, *J. Am. Chem. Soc.*, 2016, **138**, 13597–13603.
24 M. Ikeda, M. Takeuchi, S. Shinkai, F. Tani, Y. Naruta, S. Sakamoto and K. Yamaguchi, *Chem. – Eur. J.*, 2002, **8**, 5541–5550.
25 V. Marcos, A. J. Stephens, J. Jaramillo-Garcia, A. L. Nussbaumer, S. L. Woltering, A. Valero, J.-F. Lemonnier, I. J. Vitorica-Yrezabal and D. A. Leigh, *Science*, 2016, **352**, 1555–1559.
26 F. G. A. Lister, B. A. F. Le Bailly, S. J. Webb and J. Clayden, *Nat. Chem.*, 2017, **9**, 420–425.
27 R. A. Laskowski, F. Gerick and J. M. Thornton, *FEBS Lett.*, 2009, **583**, 1692–1698.
28 D. Suplatov and V. Švedas, *Acta Naturae*, 2015, **7**, 34–45.
29 S. Pedreño, J. P. Pisco, G. Larrouy-Maumus, G. Kelly and L. P. S. de Carvalho, *Biochemistry*, 2012, **51**, 8027–8038.
30 (*a*) C. Kremer and A. Lützen, *Chem. – Eur. J.*, 2013, **19**, 6162–6196; (*b*) S. Zahn, W. Reckien, B. Kirchner, H. Staats, J. Matthey and A. Lützen, *Chem. – Eur. J.*, 2009, **15**, 2572–2580.
31 I. Paul, A. Goswami, N. Mittal and M. Schmittel, *Angew. Chem., Int. Ed.*, 2018, **57**, 354–358.
32 M. L. Saha, S. Neogi and M. Schmittel, *Dalton Trans.*, 2014, **43**, 3815–3834.
33 (*a*) S. Neogi, Y. Lorenz, M. Engeser, D. Samanta and M. Schmittel, *Inorg. Chem.*, 2013, **52**, 6975–6984;

(*b*) S. Neogi, G. Schnakenburg, Y. Lorenz, M. Engeser and M. Schmittel, *Inorg. Chem.*, 2012, **51**, 10832–10841.
34 A. Ghosh, I. Paul, S. Saha, T. Paululat and M. Schmittel, *Org. Lett.*, 2018, **20**, 7973–7976.
35 H. J. Reich, *NMR Spectrum Calculations: WinDNMR, Version 7.1.13*, Department of Chemistry, University of Wisconsin.
36 M. Schmittel, H. Ammon, V. Kalsani, A. Wiegrefe and C. Michel, *Chem. Commun.*, 2002, 2566–2567.